Full length article

Characterization of Lab-on-Fiber-based dosimeters in ultra-high dose radiation fields

Patrizio Vaiano [a,1], Giuseppe Quero [a,1], Francesco Fienga [b,c,1], Valentina Di Meo [d], Pierluigi Casolaro [e], Luigi Campajola [f,g], Giovanni Breglio [b,c], Alessio Crescitelli [d], Emanuela Esposito [d], Antonello Cutolo [b], Federico Ravotti [c], Salvatore Buontempo [c,g], Marco Consales [a,*], Andrea Cusano [a,*]

[a] Optoelectronics Group - Department of Engineering, University of Sannio, I-82100 Benevento, Italy
[b] Department of Electrical Engineering and Information Technologies, University of Napoli Federico II, I-80125 Napoli, Italy
[c] European Organization for Nuclear Research (CERN), CH-1211 Genève, Switzerland
[d] Institute of Applied Sciences and Intelligent Systems, Unit of Naples, National Research Council, I-80131 Napoli, Italy
[e] Albert Einstein Center for Fundamental Physics (AEC), Laboratory for High Energy Physics (LHEP), University of Bern, CH-3012 Bern, Switzerland
[f] University of Napoli Federico II, Department of Physics, I-80126 Napoli, Italy
[g] Istituto Nazionale di Fisica Nucleare (INFN) - Sezione di Napoli, I-80126 Napoli, Italy

ABSTRACT

Next generation High Energy Physics (HEP) accelerators will require new devices and technologies capable of operating in extreme environments characterized by ultra-high radiation doses up to the MGy levels. To this aim, we report on an innovative Lab-On-Fiber (LOF) probe for the real-time dose monitoring. The proposed platform is based on a metallo-dielectric nanostructured grating made of gold and poly(methyl methacrylate) (PMMA) patterned on the termination of single mode fibers. The nanostructure has been judiciously designed to support a plasmonic resonance in the reflection spectrum occurring at near infrared wavelengths. Electron beam lithography was used for the fabrication of two LOF prototypes, which in turn, were exposed to X-rays with a total dose of 2.02 MGy and a dose rate of 88 kGy/h. Reflection spectra acquired during the irradiation revealed a clear dependence of the LOF resonance wavelength and depth on the absorbed dose, confirming the outcomes of our previous proton campaign. Morphological characterization of the irradiated samples showed that the main radiation induced effect is the reduction of the PMMA thickness (ranging between 26 % and 40 %), which in turn strongly affects the resonance behavior. Quantitative morphological measurements have been used to achieve a fair and objective correlation with our numerical modelling. Moreover, we investigated the effect of ultra-high doses of several radiation types, including X-rays, electrons and protons, on the thickness of PMMA nanolayers deposited on planar substrates. Experimental results revealed that the amount of absorbed dose (1.9–16.06 MGy) is the main parameter affecting the PMMA relative compaction (9.5–59.1 %), while the influence of the radiation type, dose rate and initial PMMA thickness can be considered negligible. Overall, these results pave the way to the development of radiation type independent PMMA assisted LOF dosimeters operating at MGy doses for the radiation monitoring in future HEP experiments.

1. Introduction

Radiation dosimetry, consisting in the measurement of absorbed dose, i.e. the energy delivered to matter by ionizing radiation per unit mass, is fundamental to ensure the control on radiation processes and safety of personnel for a wide range of areas, from industrial to medical applications. Furthermore, focusing on the field of nuclear energy and particle accelerators, accurate dosimetry prompts the timely replacement of parts, prevents disasters and keeps the instrumentation on its mettle. Europe is the home place of the largest particle accelerator, the

Large Hadron Collider (LHC), and the High Energy Physics (HEP) community is currently discussing on the next generation HEP accelerators, i.e. the Future Circular Collider (FCC), where collisions will occur at higher energy with respect to present LHC. The FCC is being designed to reach h-h collisions at unprecedented energy levels of 100 TeV, about 8 times higher than in today's LHC. As of the increased energy and luminosity, radiation levels over ten years of FCC operation in certain parts of the FCC tunnel [1] will reach tens of kGy ($>10^{15}$ particles/cm^2), and in other will exceed several tens of MGy (with $> 10^{17}$ particles/cm^2) [2]. These estimations correspond to factors of 1000 (and 100) with respect to the expected conditions at LHC and high-luminosity LHC (HL-LHC), respectively [3]. The drawback of this increase in energy is that the accelerator parts, together with the experiments that are mounted at the collision points, will accumulate radiation induced damages never experienced before. Therefore, the performance of all parts will degrade by limiting the capability for doing physics. In many cases, the material activation will be so high that rules for material handling and disposal are imposed. A detection system capable to measure that activity has the added benefit of assisting compliance with those stringent rules. Furthermore, to withstand such a harsh radiation environment, special materials and technologies are required. This implies strict components selection and development of custom qualification protocols taking into account possible dependencies of the radiation response to different technologies [4]. A survey of state-of-the-art solid-state devices for radiation measurement showed that the current existing technologies are not capable of integrating such radiation levels, as well as of providing feasible solutions to build an online radiation monitor fulfilling the FCC requirements [5]. The inherent properties of optical fibers (OFs) lend themselves to be used with great success in the ionizing radiation monitoring. OFs provide the means whereby real-time, in situ, remote monitoring of radiation doses can be realized. Being immune to electromagnetic and chemical interferences, OF sensors can be employed in harsh environments [6,7]. In addition, their very limited massive occupancy allows their positioning in regions so far prohibited to conventional dosimeters. Recently, we reported the first proof-of-principle of an alternative technology for dose monitoring in the above-mentioned scenario [8], based on the Lab-On-Fiber (LOF) technology [9–11]. Two LOF prototypes, based on a hybrid nanostructured grating made of gold and poly(methyl methacrylate) (PMMA) realized on the OF tip (OFT), were exposed at the IRRAD Proton Facility at CERN to 23 GeV protons for a total fluence of 0.67×10^{16} protons/cm^2, corresponding to an absorbed dose of 1.8 MGy. Experimental data demonstrated a clear dependence of the LOF reflected spectrum versus the total dose. The numerical analysis suggested that the main phenomenon induced by exposure to proton beam and able to explain the measured spectral behaviour is the reduction of the PMMA thickness, which is also consistent with past literature in the field [12–15]. From these findings, we carried out new numerical and experimental studies to understand the effect of the ionizing radiation on the hybrid LOF nanostructure. In particular, a new irradiation campaign has involved the online monitoring of the spectral response of two LOF prototypes exposed to X-rays for a total dose of 2.02 MGy. Atomic Force Microscopy (AFM) was adopted in order to measure the morphology changes induced by radiation in the LOF nanostructure providing relevant input for numerical modelling, thus enabling a fair and objective correlation with the achieved experimental data. Furthermore, this study provided relevant information on the effects of different types of radiation at MGy levels, including X-rays, electrons and protons, on nanometric PMMA layers deposited on planar substrates, opening to the possibility to develop optimised LOF-based dosimeters with low or even negligible dependence on the radiation type.

2. Methods

2.1. Realization of nanostructured OFT and PMMA planar substrates

The LOF prototypes used in this work are based on the integration of a hybrid nanostructured grating made of gold and PMMA on an OFT [8]. A concept scheme of the platform is shown in Fig. 1a: it consists of a nanometric holey PMMA layer on which a thin gold layer is deposited, also filling the base of the holes themselves [11], as illustrated in the inset of Fig. 1a. The morphological parameters of the nanostructure, which include the grating period, the holes radius, gold and PMMA thicknesses, have been set in order to excite localized surface plasmon resonances demonstrating a spectral dip centered at $\sim$ 1550 nm in the reflectance spectrum, which is sensitive to changes in optical properties and size of the involved materials.

The fabrication of nanostructured hybrid metallo-dielectric OFTs (shown in the scanning electron microscope (SEM) image reported in Fig. 1b) required the following steps: a) deposition of a polymeric electron resist layer, PMMA (molecular weight 950 kD, from MicroChem Corp.) onto the OFT; b) PMMA exposure, via Electron Beam Lithography (EBL), and resist development; c) gold film deposition. A uniform PMMA layer deposition in the central region of the OFTs extending for about 50 μm was ensured by the employment of a customized spin coater. In detail, a standard single mode (SMF-28) OF has been hosted in a properly pierced rotating plate, in order to achieve a uniform PMMA thickness for a region of about 50×50 μm^2, wider than the fiber core diameter ($\sim$9 μm). The EBL process has been performed with a RAITH 150 system.

An ordered holes array (Fig. 1c), designed with a period of 1050 nm and radius of 240 nm, has been exposed in the electron resist with an acceleration voltage of 20 kV, an electron beam aperture of 7.5 μm, and a dose of 100 μC/cm^2. Close to the holes array, a rectangular area (having size of 40×27 μm^2, see Fig. 1b) has been written in resist in order to realize a reference measurement area for gold thickness. After the exposure, the PMMA layer has been developed and hence covered
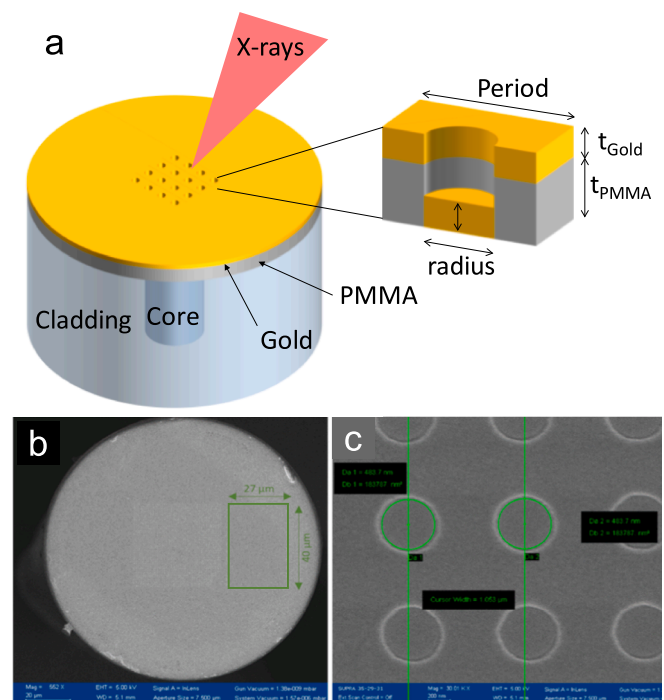

Fig. 1. a) Schematic of the LOF nanostructure realized on the OFT; b) SEM image of a realized OFT with the reference measurement area for gold thickness in right position respect to the nanopatterned area; c) detail of the hole array nanopattern.

with a nominal 50 nm thick gold film. The gold layer deposition occurs via DC magnetron sputtering, keeping the OFT perpendicular to the metal target with a properly drilled holder. In this way, the same OFT can be used for both hosting the desired array of holes and a rectangular area with only a gold film needed for evaluating the gold thickness. Furthermore, the PMMA film has been deposited, via spin coating, also on planar substrates (p-type Silicon, ⟨100⟩ orientation) to better evaluate the PMMA layer behavior when exposed to the irradiation. Planar substrates with different PMMA layer thicknesses (ranging from about 125 nm up to 390 nm) have been fabricated by varying the speed of the spin-coater (from 1000 to 3500 rpm) in order to achieve the desired thickness.

2.2. Description of the irradiation facilities and installation of the samples

To understand the behaviour of the proposed LOF dosimeter and to deepen the knowledge of the physical phenomena involved in the experienced spectrum variations when the LOF prototypes are exposed to ionizing radiation, an extended experimental campaign has been specifically designed and carried out. In particular, two LOF sensors have been exposed to X-rays up to 2.02 MGy, while several samples consisting of nano-scale layers of PMMA, deposited on planar substrates, have been irradiated at different doses ranging between 1.9 MGy and 16.06 MGy with protons, electrons and X-rays. In the following, a brief description of the radiation sources is given; a summary of the main features of the irradiation facilities involved in this work is reported in Table 1. Three PMMA samples have been exposed to a 2 MeV electron beam from ILU-6 LINAC of the Institute of Nuclear Chemistry and Technology (INCT) in Warsaw (Poland). The samples were placed on the surface of an Aluminum (Al) plate positioned at 72 cm from the output window of the accelerator. The dose on the sample position is proportional to the charge delivered on the Al-plate [16]. The dose rate in the film position was evaluated to be 367 kGy/h, whereas the total delivered dose was 1.9 MGy. The total dose at the end of the irradiation was double-checked with radiochromic film dosimetry [17]. Other PMMA samples have been exposed to a 10 MeV proton beam from the tandem accelerator of INFN Laboratori Nazionali del Sud (LNS) in Catania (Italy). The irradiation was performed by extracting the beam in air and by monitoring the proton fluence rate in the sample position, by measuring the beam current with a specific ionization chamber designed for this purpose [18,19]. The total dose delivered to the sample was found to be 1.9 MGy and the dose rate 277 kGy/h.

Finally, two LOF sensors and four PMMA samples have been exposed to X-rays from the CERN ObeliX machine in Genève (Switzerland), composed of a Seifert RP149 X-ray machine, a rectangular thermal plate and a Huber Unistat 705 cooling element. The X-ray tube is equipped with a beryllium window thick 0.25 mm to seal the tube, and an Al-filter of 0.15 mm to ensure reasonably uniform dose rate in the device under test (DUT). The preliminary calibration is performed with a Quantrad PIN diode. During the irradiation experiments, the X-ray tube power supply voltage was set to 50 kV, and the current to 60 mA. In the position where the DUTs were placed the dose rate was 88 kGy/h. The total dose delivered to the LOF prototypes was 2.02 MGy, while the planar samples were exposed to different doses ranging between 2.02 MGy and 16.06

MGy.

3. Experimental results and discussion

3.1. LOF spectral response to X-rays irradiation

Two LOF prototypes have been exposed to X-rays at the ObeliX irradiation system at CERN with an average dose rate of 88 kGy/h and a total dose of 2.02 MGy. In order to get a real-time measurement of the radiation induced effects of the X-rays on the LOF nanostructures, the reflectance spectra of the two LOF samples were continuously acquired by using a commercial sm125 Optical Sensing Interrogator (Micron Optics Inc.), featuring the wavelength range 1510–1590 nm with an accuracy of 1 pm. The spectra were saved on a personal computer with a time interval of 3 min and processed using a Matlab® script for filtering and tracking the main changes occurred in the resonance wavelength and visibility (i.e. the valley depth, computed as the difference between the spectrum baseline evaluated far from the valley and the minimum). Fig. 2a and b show some selected reflectance spectra of the prototypes 1 and 2, respectively, during the exposure to X-rays. The legends indicate the elapsed time since the start of the monitoring and the accumulated dose, whose behaviour is also described through a color bar on the right. The spectral monitoring phase started 2 h before the beam was switched on and terminated about 35 h after the end of the irradiation. The blue lines indicate the spectra of the two LOF samples before the irradiation. The main difference between them is in the visibility of the resonant valley, which is 1.5 dBm for prototype 1 and 4.5 dBm for prototype 2, mainly due to the difference in thickness of the PMMA layers, as demonstrated through AFM measurements reported in the next section.
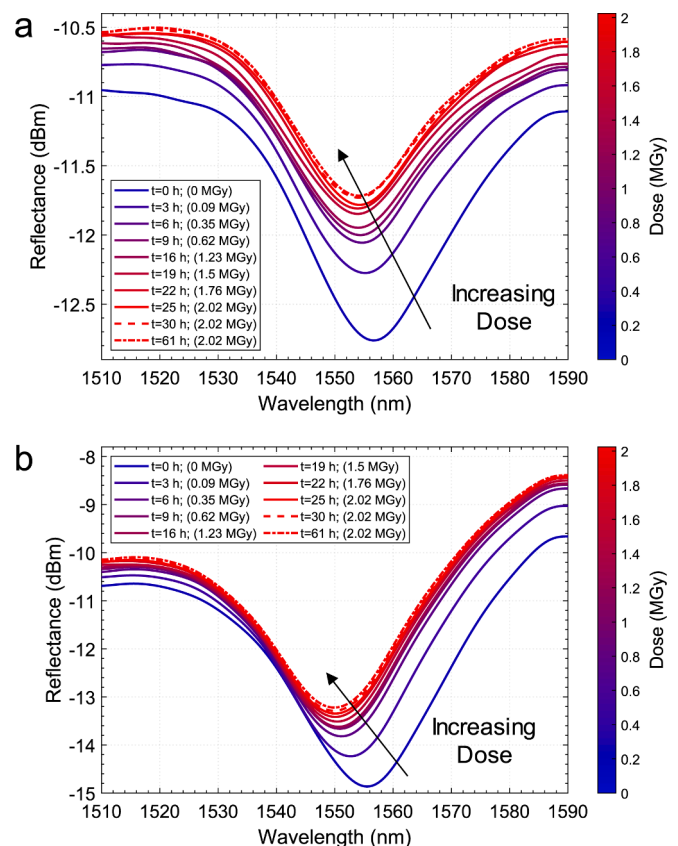

Table 1
Main characteristics of the radiation facilities involved in this work.

Facility	Radiation type	Dose-rate (kGy/h)	Dose[a] (MGy)
ObeliX machine at CERN, Genève	X-rays	88	2.02–16.06
Accelerator of LNS-INFN, Catania	10 MeV Protons	266	1.9
ILU-6 LINAC of INCT, Warsaw	2 MeV Electrons	367	1.9

[a] Dose referred to Silicon.

Fig. 2. Evolution of the reflectance spectra during the exposure to X-rays for a) LOF prototype 1 and b) prototype 2. The first (blue) spectrum refers to the pre-irradiation phase, while the last two (red) spectra refer to the post-irradiation phase. (For interpretation of the references to color in this figure legend, the reader is referred to the web version of this article.)

The main evidences arising from the two plots in Fig. 2 are a blue shift of the resonant dip and an increase in reflectivity in the whole spectrum, which is more noticeable in correspondence with the valley, thus leading to a reduction in its depth.

These two phenomena are described quantitatively in Fig. 3a and b, which report the radiation induced (barycentral) resonance wavelength shift ($\Delta\lambda_b$) and visibility reduction as a function of the radiation time. In order to facilitate the understanding of the response of the two sensors to radiation, the same graphs also indicate the accumulated dose on the right vertical axis. With the aim of comparing the responses of the two devices, the variations with respect to the starting values are shown on the ordinates, instead of their absolute values. Three phases can be clearly distinguished: pre-irradiation, X-rays irradiation and post-irradiation. In the pre-irradiation phase (0–2 h), the spectrum did not undergo significant changes. This phase provided a reliable starting level for evaluating the subsequent variations induced by radiation. During the irradiation (2–25 h), a progressive blue shift of the resonance wavelength and a reduction of the visibility can be observed. In the first few hours of exposure to X-rays, the two LOF samples showed an almost overlapped behavior, while after about 3 h of irradiation they revealed a different sensitivity to the absorbed dose, which can be attributed to their different original morphology. An unexpected shutdown of the computer used for the spectral monitoring caused the loss of information for about 4 h during the irradiation (9–13 h), as clearly observable in the interval with no markers in Fig. 3a and b.

Nonetheless, when monitoring was resumed, the measured trend was found consistent with the one prior to the interruption, demonstrating that this event did not affect the experiment. At the end of the irradiation phase (25 h), the measured blue shift was 2.2 nm for prototype 1 and 5.6

nm for prototype 2. In addition, a reduction in dip visibility equal to 0.55 dBm for prototype 1 and 0.95 dBm for prototype 2 was detected. Finally, the monitoring after the beam was switched off (25–60 h) revealed a limited variation in the wavelength, respectively of + 0.2 nm and –0.5 nm for prototypes 1 and 2, and a further reduction in the visibility of about 0.1 dBm for both devices. The response in terms of wavelength shift and visibility reduction of the resonance valley with respect to the dose was built by assuming a constant dose rate (88 kGy/h) for the duration of exposure to X-rays and is shown in Fig. 4. Both devices have been shown to withstand a dose of 2.02 MGy while retaining their spectral characteristics. In both plots the two sensors have a very similar response for low doses (up to a few hundred kGy), while for higher doses the variations recorded by prototype 2 are larger. The wavelength changes in device 1 (Fig. 4a) reached a substantial saturation after 1.6 MGy, while the visibility (Fig. 4b) continued to vary, suggesting that the LOF structure continues to change even for higher doses.

3.2. Morphological characterization of LOF prototypes

In order to fully understand the morphology changes in the LOF nanostructure induced by radiation and how they would affect its resonant behaviour, a complete morphological characterization has been carried out before and after 2.02 MGy X-ray irradiation. In particular, AFM measurements (Agilent Technologies 5420, Agilent Technologies, Santa Clara, CA) were carried out in order to estimate the thickness of gold and PMMA layers before and after the irradiation
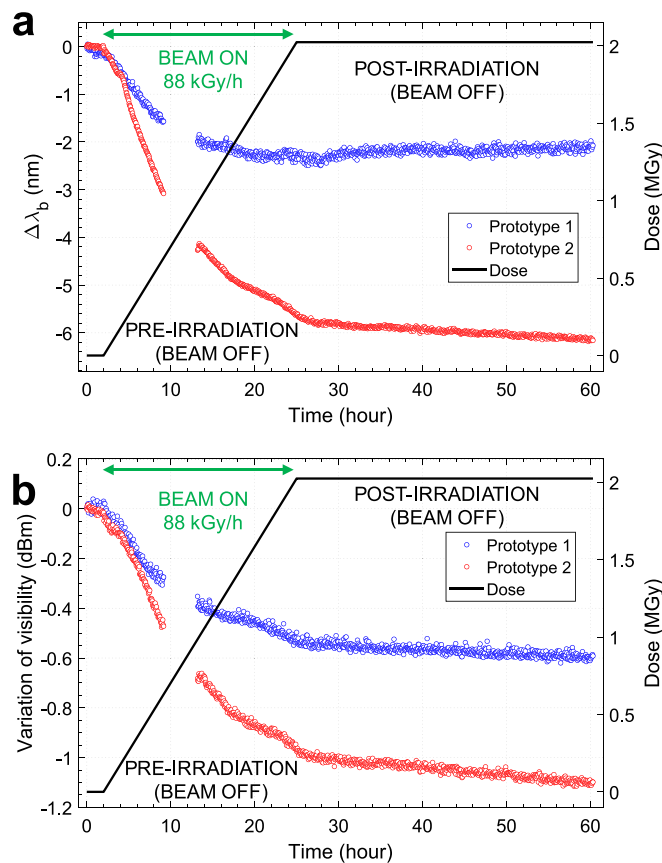
Fig. 3. Time-response of the LOF prototypes during the experiment, which includes pre-irradiation, X-rays irradiation and post-irradiation phases. a) Radiation induced wavelength shift and b) visibility reduction as a function of the time.
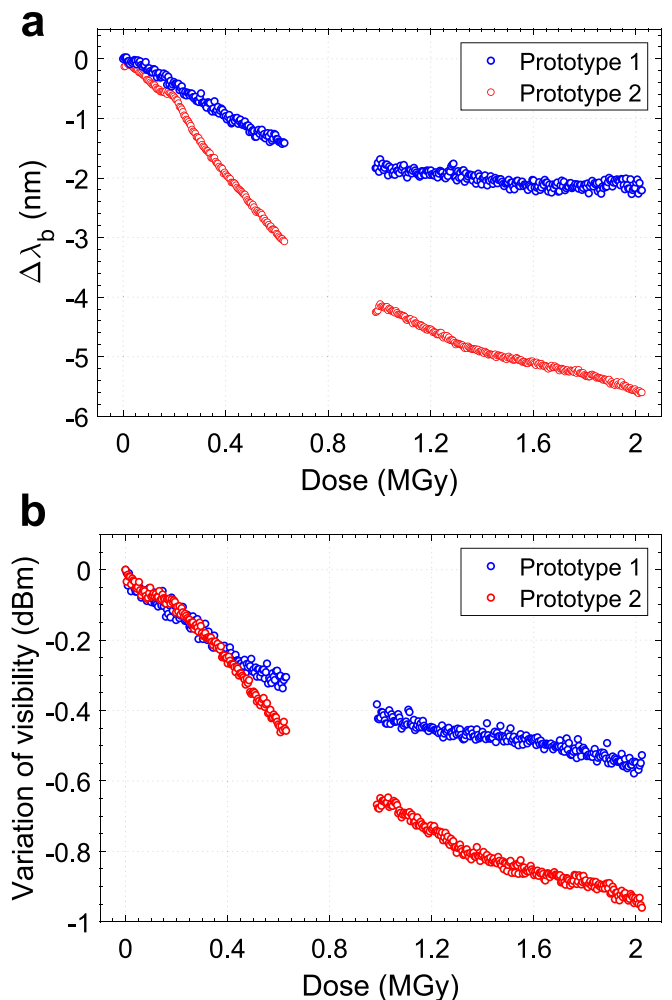
Fig. 4. a) Radiation induced wavelength shift and b) visibility reduction of LOF prototypes exposed to X-rays with a dose rate of 88 kGy/h up to 2.02 MGy.

process. AFM characterizations were performed directly onto the OFT in no-contact mode in order to prevent damage of the patterned nanostructure, by keeping fixed the fiber in a customized holder. To measure the gold thickness, a region of 10×10 μm^2 was ablated in the 40×27 μm^2 rectangular area (covered only by gold) located between the center and the edge of the OFT (Fig. 1b). The region to be ablated was chosen as far away from the pattern as possible to ensure that the removed material did not redeposit on the patterned region. The ablation process was performed by means of an excimer laser (OPTEC LB 1000) working at a wavelength of 248 nm, with a pulse width of about 5–6 ns [20]. A plastic holder keeps the OF facet perpendicular to the laser beam during the ablation process. The laser energy used is 3 mJ and the repetition rate is 50 Hz. The measurement of the PMMA thickness was performed by AFM analysis of the holes depth in the patterned area. An extract of the images produced as part of this morphological characterization is shown in Figs. 5 and 6. In particular, Fig. 5a contains a SEM top view image of LOF prototype 1 before irradiation, highlighting the rectangular area, in which the gold layer was ablated in order to evaluate its thickness. Fig. 5b shows the AFM profile of the ablated region, revealing a substantial X-ray radiation independence of the gold average thickness, which measures 51.6 ± 1.6 nm and 51.1 ± 1 nm, respectively before and after the irradiation. As evident from Fig. 5b, the region affected by the redeposition of gold extends only for ~ 1 μm, therefore it is far enough away from the pattern not to affect it. Moreover, since the peaks due to the redeposition effect shown in Fig. 5b and 6b are irregular and dependent on the repeatability of the positioning of the samples during the AFM measurement, their profile has not been considered for the estimation of the gold thickness, which is evaluated in the adjacent flat regions.

Fig. 5c and 6d show an AFM 3D image and the 2D profile of a portion of the nanopatterned area of prototype 1 before X-ray irradiation, while Fig. 5e and 5f refer to the AFM analysis performed after irradiation. Due to the substantial radiation independence of the gold thickness, the AFM profile obtained through the holes of the nanostructure corresponds to the actual PMMA thickness. By analyzing these images, the PMMA thickness was found to vary from 78.3 ± 2.5 nm to 58 ± 1.3 nm, demonstrating a compaction effect of the PMMA as response to X-ray irradiation. The associated PMMA thickness percentage reduction (Δt_{PMMA}) was evaluated according to the following expression:

where, t_{PMMA_unirr} and t_{PMMA_irr} were the PMMA thickness before and after the irradiation process, respectively. For the prototype 1, Δt_{PMMA} was evaluated to be 26 %. Similarly, a complete morphological characterization has been carried out before and after the irradiation also for LOF prototype 2, as shown in Fig. 6. In particular, a gold average height of 49.9 ± 1.6 nm and 49.3 ± 1 nm was registered before and after the irradiation (Fig. 6b). The PMMA thickness before the irradiation process was 130 ± 3 nm (Fig. 6c and 6d). Finally, Fig. 6e and 6f show an AFM image and a profile of the structure after the X-ray irradiation. As evident from the AFM analysis, in this case the X-ray radiation heavily modified the nanopattern, which at the end of the exposure presents an irregular structure characterized by some filled holes. However, by considering the deepest holes, a PMMA thickness after the irradiation equals to 79.3 ± 3 nm and a Δt_{PMMA} of 40 % can be estimated. In conclusion, the AFM analysis carried out before and after irradiation showed that, while the gold thickness layer remains almost unchanged, the irradiation impact is more evident for the PMMA thickness, which has shown a relative reduction of 26 % and 40 % for the LOF prototype 1 and 2, respectively. Overall, these experimental evidences related to the PMMA thickness variations allowed us to confirm the hypothesis formulated in our previous work [8], where through numerical simulations, the compaction of PMMA was recognized as the most accredited reason of the spectral variations reported by LOF sensors exposed to protons at MGy level.

Another evident aspect is the different Δt_{PMMA} percentage undergone by the two LOF prototypes exposed to the same X-ray dose of 2.02 MGy. This result is most probably due to the different PMMA thickness before the irradiation of the two LOF prototypes. In particular, Figs. 5 and 6 also demonstrate that both the PMMA compaction and the radiation induced degree of distortion in the nanopatterned structure increase when the PMMA layer is thicker. The deformation of the LOF nanostructure as an effect of PMMA compaction suggests that the morphological changes induced by ionizing radiation may differ depending on the structure of the device. In particular, in an interdigitated structure such as that of LOF sensors, the deformation of the PMMA induced by radiation will be different compared to the same material deposited on a planar surface and therefore with more degrees of freedom.
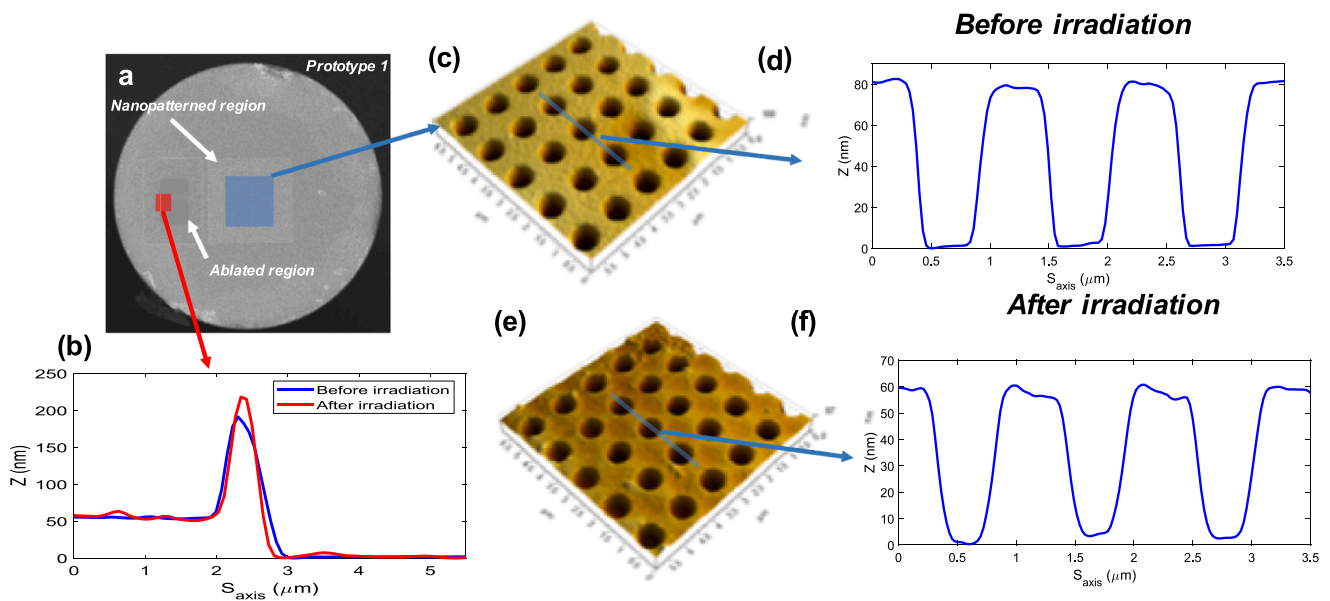
$$\Delta_{tPMMA} \, [\%] = 100 \times (t_{PMMA\_unirr} - t_{PMMA\_irr}) \, / \, t_{PMMA\_unirr} \qquad (1)$$

Fig. 5. Morphological characterization of the LOF prototype 1: a) SEM image of OFT before irradiation with highlighted the nanopatterned and ablated regions; b) AFM cross-section of the gold before and after irradiation; nanopattern AFM topography and PMMA profile before c, d) and after e, f) X-rays irradiation.

Fig. 6. Morphological characterization of the LOF prototype 2: a) SEM image of OFT before irradiation with highlighted the nanopatterned and ablated regions; b) AFM cross-section of the gold before and after irradiation; nanopattern AFM topography and PMMA profile before c, d) and after e, f) X-rays irradiation.
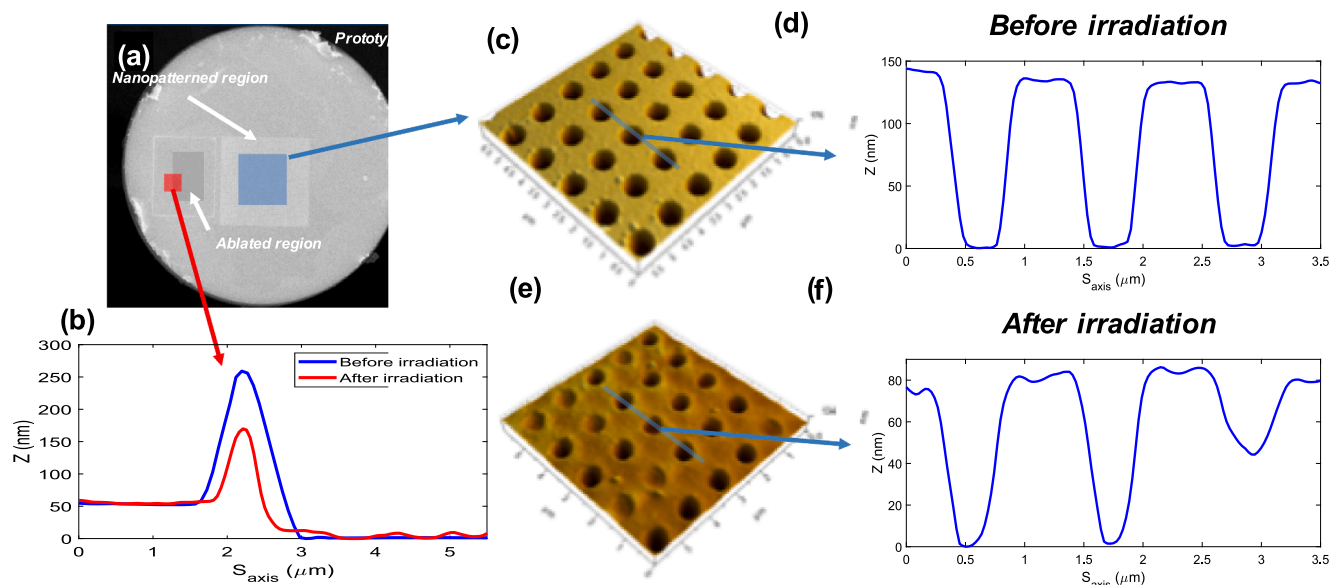
3.3. Numerical simulations

The knowledge of the morphological parameters of the pattern before and after the exposure to X-rays enabled us to correctly model the nanostructure, and to correlate the radiation induced morphological changes with spectral reflectance modifications, allowing a fair comparison with the achieved experimental data. By adopting the finite element method provided by the Comsol Multiphysics RF module, the parameters shown in Table 2 and 3 were used to simulate the spectra before and after exposure, following the same approach described in a previous work [8].

In particular, the spectra before the irradiation were computed by using the period and radius of the holes measured by analyzing the SEM images and the thicknesses of gold and PMMA measured by analyzing the AFM images. As can be seen in Fig. 7, the numerical spectra based on the geometrical parameters measured before the irradiation have a minimum located around 1550 nm, while the visibility of prototype 1 is lower than prototype 2 due to its lower PMMA thickness, as also confirmed by the experimental spectra reported in Fig. 2. AFM measurements performed after irradiation made it possible to modify the thickness of gold and PMMA in the simulation compared to the initial values, while keeping constant the radius and period. Based on these parameters, the numerical analysis reveals that X-ray exposure determines a blue shift of the resonance (2.5 and 6.9 nm for prototypes 1 and 2, respectively), a reduction in visibility and an increase in the baseline, especially on the right edge of the resonance. These three phenomena are all consistent with the experimental spectral changes shown in Fig. 2. In addition, prototype 2, which underwent a larger reduction in the thickness of the PMMA layer (~50 nm), exhibited greater variation in all three parameters, confirming the agreement with the experimental data.

Table 2
Morphological parameters of the LOF prototype 1 before and after the X-ray irradiation.

Parameter	Before exposure	After exposure
Period (nm)	1047	–
Radius (nm)	245.25	–
t_{gold} (nm)	51.6 ± 1.6	51.1 ± 1
t_{PMMA} (nm)	78.3 ± 2.5	58 ± 1.3 (–26 %)

Table 3
Morphological parameters of the LOF prototype 2 before and after the X-ray irradiation.

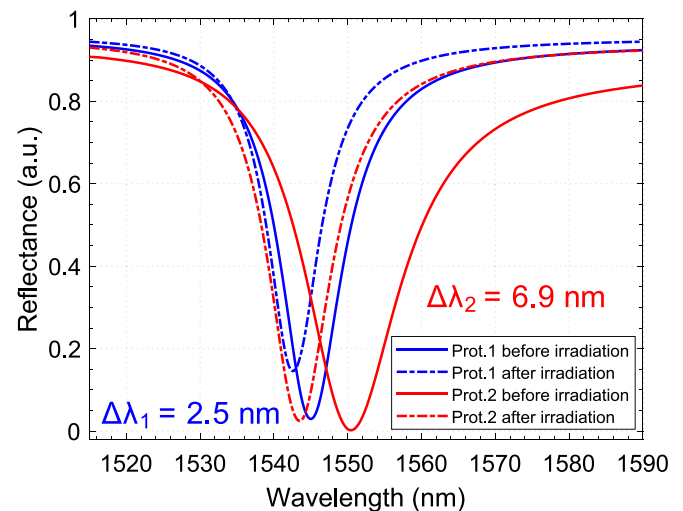| Parameter	Before exposure	After exposure
Period (nm)	1046	–
Radius (nm)	241.5	–
t_{gold} (nm)	49.9 ± 1.6	49.3 ± 1
t_{PMMA} (nm)	130 ± 3	79.3 ± 3 (–40 %)

Fig. 7. Numerical simulation of the reflectance spectra based on the experimental measurements of morphological parameters of the two LOF prototypes before and after the X-ray irradiation. The linear scale was preferred to the logarithmic one in order to appreciate also the variations of the baseline.

In quantitative terms (see Table 4), the shifts estimated by the simulations differ from the experimental ones by 0.3 nm (12 %) for prototype 1, and 1.3 nm (19 %) for prototype 2. The larger discrepancy from numerical simulations exhibited by prototype 2 may be associated to the more notable structural changes induced by radiation, which made, as observed in the previous section, its post-irradiation pattern no longer

Table 4
Simulated and experimental wavelength shift of the LOF prototypes after the X-ray irradiation.

LOF Prototype	Simulated $\Delta\lambda$ (nm)	Experimental $\Delta\lambda$ (nm)
1	2.5	2.2
2	6.9	5.6

regular.

3.4. Radiation induced variation of PMMA thickness on planar substrates

The experimental and numerical analysis carried out in this work suggests that the spectral variations reported by LOF sensors under X-rays irradiation at MGy level are dominated by the changes in the PMMA thickness. Moreover, the response of LOF prototypes to X-rays turned out to be very similar to that reported by the same type of sensors to high energy protons [8]. These evidences prompted us to verify the effect of different types of radiation at MGy level on the PMMA thickness in planar substrates, in which the PMMA is able to change with greater freedom compared to the constrained structure of LOF devices. The effect of high energy irradiation on the properties of polymeric materials is complex and is dependent on the chemical nature of the repeat chain molecules unit, molecular weight, polymeric state, initial degree of polymer crystallinity. The rate of irradiation, processing temperature and atmosphere during irradiation are important factors influencing the intensity of the effects [21]. The radiation damage on the polymer occurs through the interaction with a high-energy electron, which is a complex and random process; these electrons have energy much greater than the binding energies of the electrons bound to the molecules of the polymer [22]. During the irradiation, the polymer undergoes scission of the main chain and the creation of free radicals, unsaturation (double bonds), crosslinks, and end-links, as a result of the secondary electrons that are formed during the decay energy cascade. With the aim of investigating the X-ray absorbed dose effect on the PMMA layer thickness, a morphological analysis of several PMMA nanometric planar samples before and after the X-ray irradiation has been carried out. As described for LOF prototypes, also the PMMA layers deposited on the planar samples were ablated via excimer laser in order to realize a square hole of $10 \times 10 \ \mu m^2$ at the center of the sample, useful for evaluating the thickness before and after the irradiation. As shown in Table 5, four samples were tested at CERN ObeliX machine for different X-ray doses ranging from 2.02 MGy to 16.06 MGy and a dose rate of 88 kGy/h. In particular, two samples, characterized by a PMMA thickness (before irradiation) of 125 ± 2.1 nm and 132 ± 1.2 nm, were exposed to a total dose of 2.02 MGy, which corresponds to the same value adopted
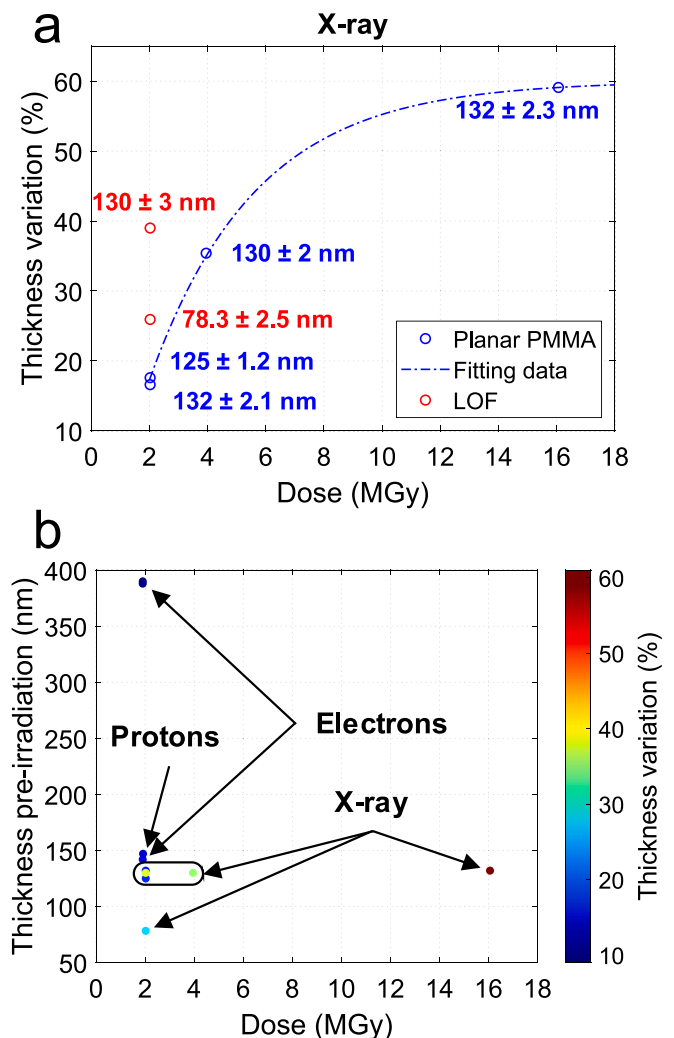
for the LOF prototypes. The percentage compactions observed after the exposure were 17.6 % and 16.6 %, respectively. In order to explore the effects of higher dose levels, two further samples, characterized by a PMMA thickness (before irradiation) of 130 ± 2 nm and 132 ± 2.3 nm, were exposed to a total dose of 3.95 MGy and 16.06 MGy, leading to thickness percentage changes of 35.4 % and 59.1 %, respectively.

The relative percentage reduction of the thickness in planar substrates of PMMA exposed to X-rays as a function of the dose is shown in Fig. 8a, demonstrating that an increase of the absorbed dose at MGy scale causes an increment of the PMMA relative compaction. These results are thus consistent with the online monitoring of the LOF prototypes spectral variations that occur as a consequence of the progressive PMMA compaction and pave the way to the development of a new class of LOF dosimeters which can be used in ultra-high dose environments. For the sake of fullness, the percentage change in PMMA thickness of the two LOF prototypes has been added to Fig. 8a. The discrepancy between LOF and planar samples confirms the above-mentioned hypothesis about the influence of the metal-dielectric inter-digitated LOF structure on the compaction phenomenon in the polymer with respect to the flat PMMA layer. The obtained results indicate that there are still open points regarding the effect of radiation on complex hetero-structures (as the case of LOF platforms). At the same time, the

Table 5
Thickness of PMMA planar substrates before and after the irradiation.

Radiation type	Dose[b] (MGy)	Dose-rate (kGy/h)	t_{PMMA} before exposure (nm)	t_{PMMA} after exposure (nm)	Relative Compaction[c] [%]
X-rays	2.02	88	125 ± 2.1	103 ± 2	17.6
X-rays	2.02	88	132 ± 1.2	110 ± 2	16.6
X-rays	3.95	88	130 ± 2	84 ± 2	35.4
X-rays	16.06	88	132 ± 2.3	53 ± 3	59.1
10 MeV Protons	1.9	266	147 ± 2.5	128 ± 4	12.9
2 MeV Electrons	1.9	367	142 ± 1.8	121 ± 3	14.7
2 MeV Electrons	1.9	367	388 ± 3.1	350 ± 3	9.8
2 MeV Electrons	1.9	367	390 ± 3.1	353 ± 3	9.5

[b] Dose referred to Silicon. [c] The relative compaction is evaluated according to Equation (1).

Fig. 8. a) Relative reduction of the thickness in planar substrates of PMMA and LOF prototypes exposed to X-rays as a function of the dose; b) Relative reduction of the thickness (color bar) in planar substrates of PMMA and LOF prototypes exposed to different types of radiation (electrons, protons and X-rays) as a function of the dose and of the PMMA thickness before irradiation.

present work opens interesting avenues towards the development of low cost and effective micro and nano PMMA-assisted optical dosimeters for HEP.

The investigation of the PMMA thickness percentage reduction in planar substrates has been extended to different types of radiation, including also protons and electrons, as reported in Table 5. In particular, a PMMA planar sample with a thickness before irradiation of 147 ± 2.5 nm was exposed to a 10 MeV proton beam from tandem accelerator of LNS-INFN in Catania for a total absorbed dose of 1.9 MGy (dose rate of 266 kGy/h). In this case, the relative percentage reduction of the PMMA thickness was 12.9 %, very close to the compaction registered for X-rays at a similar dose (2.02 MGy). Three PMMA planar samples with very different thicknesses (142 ± 1.8 nm, 388 ± 3.1 nm and 390 ± 3.1 nm) were also exposed to a 2 MeV electron beam from ILU-6 LINAC of INCT in Warsaw, receiving a total dose of 1.9 MGy (dose rate of 367 kGy/h) and registering a relative percentage reduction of the PMMA thickness of 14.7 %, 9.8 % and 9.5 %, respectively. Also, the relative percentage reduction of the PMMA thickness is comparable to the compaction measured for the samples exposed to X-rays at a similar dose (2.02 MGy). Fig. 8b shows the relative reduction of the thickness (colorbar) in PMMA planar substrates exposed to different types of radiations (X-rays, electrons and protons) as a function of the dose and of the PMMA thickness before irradiation. The first evidence of this comparison is that the PMMA relative compaction is mostly due to the amount of absorbed dose in respect to the influence of the radiation type, as confirmed by the two samples exposed at about 4 and 16 MGy, which underwent the highest thickness reduction of 35.4 % and 59.1 %, respectively. Differently, all the samples exposed to a dose ranging between 1.9 and 2.02 MGy showed an average reduction of the PMMA thickness of 13.5 % with a standard deviation of 3.4 %, demonstrating a substantial independence on both the radiation type/dose rate and PMMA thickness before the irradiation.

A possible explanation of the experimental phenomena reported here can be provided bearing in mind the chemical structure of PMMA represented in Fig. 9. In particular, the relative reduction of the thickness of a layer of PMMA deposited on a silicon substrate when the absorbed dose increases under X-rays irradiation shown in Fig. 8a is consistent with the degradation of the chemical structure of PMMA via chain scission (that makes PMMA ideally suited as electron-resist).

Our PMMA is characterized by a high value of molecular weight (MW = 950000) and this aspect gives an increase in the efficiency of the chain scission effect. These radiation damage processes lead to a mass reduction (decrease of C = O bonds density) [23–26] and therefore to a thinning of the thicknesses, with the increasing dose. Moreover, the main interaction of the radiation with the polymer is due to secondary electron with low energy (about 10 eV), therefore the radiation damage does not depend on the type of the primary impinging particle as shown from Fig. 8b.

4. Conclusions

In this work we reported on an innovative online LOF-based dosimeter capable of operating in scenarios characterized by ultra-high dose ionizing radiation. In particular, we experimentally confirm
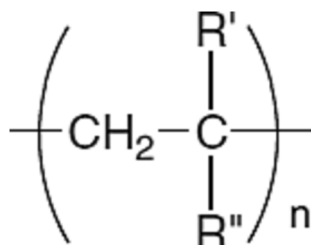

Fig. 9. Chemical structure of PMMA (R′ =CH3, R″ = COOCH3).

the findings of our first investigation with LOF-based dosimeters exposed to 24 GeV protons. In this work, we performed several irradiation campaigns aimed at deepening the understanding of the radiation effects at MGy dose levels on the spectral response of LOF dosimeters, especially taking into account the complexity of the metallo-dielectric nanostructure patterned on the OFT. A complete morphological characterization involving SEM and AFM measurements provided the precise geometry of the tested LOF samples before irradiation, showing in particular a thickness of the PMMA layer of 78.3 and 130 nm, respectively in prototypes 1 and 2. Two LOF-based dosimeters were exposed to X-rays for a total dose of 2.02 MGy, reporting a blue shift of the resonance wavelength of 2.2 and 5.6 nm and a reduction in dip visibility of 0.55 and 0.95 dBm, respectively for prototype 1 and 2. Post-irradiation AFM measurements revealed that PMMA thickness decreased by 26 and 40 %, respectively. These results allowed us to draw some relevant considerations. First of all, the spectral variations induced by X-rays are consistent with those previously observed under protons at similar doses. Moreover, the hypothesis formulated in our previous work about the compaction of the PMMA layer as the main phenomenon induced by ionizing radiation is now experimentally confirmed by the AFM measurements. Furthermore, the LOF sample with the higher initial PMMA thickness has shown larger spectral variations, percentage reduction in PMMA thickness and degree of distortion of the nanostructure with respect to the other sample having a thinner PMMA layer. Morphological measurements of the irradiated samples were also exploited as input for numerical modelling, enabling a fair and objective correlation with experimental data. The slight disagreement between simulated and acquired spectra can be explained by the radiation induced deformation of the LOF nanostructure, in turn due to the compaction of the PMMA, which is unequivocally conditioned by the interdigitated LOF structure. We further studied the effect of different types of radiation at MGy level on the thickness of nanometric planar substrates, in which the PMMA is able to change with greater freedom compared to the constrained structure of LOF devices. The irradiation campaigns on PMMA planar substrates, including X-rays, electrons and protons, demonstrated that the amount of absorbed dose (ranging between 1.9 and 16.06 MGy) is the foremost parameter responsible of the PMMA relative compaction (from 9.5 to 59.1 %), while the influence of the radiation type, dose rate and initial PMMA thickness is negligible. In a future perspective, the results achieved in the present work allow to set the main guidelines for the development of a new class of LOF-based dosimeters with a low or even negligible radiation type dependence for the real-time monitoring in HEP experiments.

CRediT authorship contribution statement

Patrizio Vaiano: Methodology, Investigation, Software, Formal analysis, Data curation, Writing – original draft, Writing – review & editing. **Giuseppe Quero:** Methodology, Investigation, Software, Formal analysis, Data curation, Writing – original draft, Writing – review & editing. **Francesco Fienga:** Conceptualization, Supervision, Methodology, Investigation, Writing – original draft, Writing – review & editing. **Valentina Di Meo:** Methodology, Resources, Investigation, Writing – original draft, Writing – review & editing. **Pierluigi Casolaro:** Methodology, Investigation, Writing – original draft, Writing – review & editing. **Luigi Campajola:** Conceptualization, Supervision, Investigation, Writing – review & editing. **Giovanni Breglio:** Conceptualization, Supervision, Investigation, Writing – review & editing. **Alessio Crescitelli:** Methodology, Resources, Investigation, Writing – original draft, Writing – review & editing. **Emanuela Esposito:** Supervision, Methodology, Resources, Investigation, Writing – original draft, Writing – review & editing. **Antonello Cutolo:** Conceptualization, Supervision, Investigation, Writing – review & editing. **Federico Ravotti:** Conceptualization, Supervision, Methodology, Investigation, Writing – review & editing. **Salvatore Buontempo:** Conceptualization, Supervision, Investigation, Writing – review & editing. **Marco Consales:**

Conceptualization, Supervision, Investigation, Writing – review & editing. **Andrea Cusano:** Conceptualization, Supervision, Investigation, Writing – review & editing.

Declaration of Competing Interest

The authors declare that they have no known competing financial interests or personal relationships that could have appeared to influence the work reported in this paper.

Data availability

Data will be made available on request.

Acknowledgements

References

[1] A. Infantino, R. Alía, M. Besana, M. Brugger, F. Cerutti, EPJ Web Conf. 153 (2017) 03004.
[2] M. Besana, F. Cerutti, A. Ferrari, W. Riegler, V. Vlachoudis, Phys. Rev. Accel. Beams 19 (2016), 111004.
[3] G. Apollinari, O. Brüning, T. Nakamoto, L. Rossi, "High-Luminosity Large Hadron Collider. Technical Design Report," CERN-2015, 2015, 5.
[4] B. Camanzi, A. Holmes-Siedle, Nat. Mater. 7 (2008) 343–345.
[5] A. Abada, M. Abbrescia, S.S. AbdusSalam, C. Biscari, EPJ Special Topics 228 (4) (2019) 755–1107.
[6] A. Chiuchiolo, M. Bajko, J. Perez, H. Bajas, M. Consales, M. Giordano, G. Breglio, A. Cusano, IEEE Photonics J. 6 (2014) 1–10.
[7] F. Fienga, Z. Szillasi, N. Beni, A. Irace, A. Gaddi, W. Zeuner, A. Ball, S. Buontempo, G. Breglio, Opt. Laser Technol. 120 (2019), 105650.
[8] G. Quero, P. Vaiano, F. Fienga, M. Giaquinto, V. Di Meo, G. Gorine, P. Casolaro, L. Campajola, G. Breglio, A. Crescitelli, E. Esposito, A. Ricciardi, A. Cutolo, F. Ravotti, S. Buontempo, M. Consales, A. Cusano, Sci. Rep. 8 (2018) 1–13.
[9] A. Cusano, M. Consales, A. Crescitelli, A. Ricciardi, Lab-on-fiber technology, Springer International Publishing, 2015.
[10] A. Ricciardi, M. Consales, G. Quero, A. Crescitelli, E. Esposito, A. Cusano, ACS Photonics 1 (2013) 69–78.
[11] M. Consales, A. Ricciardi, A. Crescitelli, E. Esposito, A. Cutolo, A. Cusano, ACS Nano 6 (2012) 3163–3170.
[12] W. Hong, H. Woo, H. Choi, Y. Kim, G. Kim, Appl. Surf. Sci. 169–170 (2001) 428–432.
[13] H. Choi, H. Woo, W. Hong, J. Kim, S. Lee, C. Eum, Appl. Surf. Sci. 169–170 (2001) 433–437.
[14] T. Sum, A. Bettiol, C. Florea, F. Watt, J. Lightwave Technol. 24 (2006) 3803–3809.
[15] T. Sum, A. Bettiol, H. Seng, I. Rajta, J. van Kann, F. Watt, Nucl. Instrum. Meth. B 210 (2003) 266–271.
[16] P. Vaiano, M. Consales, P. Casolaro, L. Campajola, F. Fienga, F. Di Capua, G. Breglio, S. Buontempo, A. Cutolo, A. Cusano, Phys. Med. 61 (2019) 77–84.
[17] P. Casolaro, L. Campajola, F. Capua, J. Instrum. 14 (2019) P08006–P.
[18] G.A.P. Cirrone, G. Cuttone, D. Battaglia, L. Calabbretta, F.D. Rosa, P. Lojacono, Polish, J. Environ. Stud. 15 (4A) (2006) 171–173.
[19] L. Campajola, P. Casolaro, F. Capua, J. Instrum. 12 (2017) P08015–P.
[20] G. Quero, A. Crescitelli, D. Paladino, M. Consales, A. Buosciolo, M. Giordano, A. Cutolo, A. Cusano, Sensor. Actuat. B-Chem. 152 (2011) 196–205.
[21] K. Dawes, L. C. Glover, D. A. Vroom, in Physical properties of polymers handbook, Springer, New York, NY, 2007, 867-887.
[22] A.P. Smith, R.J. Spontak, H. Ade, Polym. Degrad. Stabil. 72 (2001) 519–524.
[23] T. Beetz, C. Jacobsen, J. Synchrotron Radiat. 10 (2003) 280–283.
[24] P. Silva, C. Albano, R. Perera, N. Domínguez, Radiat. Phys. Chem. 79 (3) (2010) 358–361.
[25] S. Iqbal, M.S. Rafique, S. Anjum, A. Hayat, N. Iqbal, Appl. Surf. Sci. 259 (2012) 853–860.
[26] J. Spiga, J. A. Duffy, P. Pellicioli, S. Manger, A. Bravin, 2018 IEEE Nucl. Sci. Symposium and Medical Imaging Conference Proceedings (NSS/MIC), 2018, 1-3.